Published in AJSE, Vol: 25, Issue:1
Received on 19th May 2025
Revised on 19th August 2026
Published on 31st August 2026

AIUB JOURNAL OF SCIENCE AND ENGINEERING
ISSN: 1608 - 3679 (print) 2520 - 4890 (Online)
https://doi.org/10.53799/sj1pdd74

Numerical Simulation and Optimization of Lead-Free $CsGeI_2Br/FASnI_3$ Dual-Absorber Perovskite Solar Cell with Organic Charge Transport Layer

Md Abid Morshed, Mohammad Abdul Mannan, Md Rifat Hazari

***Abstract*— As demand grows for high-efficiency, affordable, and eco-friendly photovoltaic technology, alternative materials such as $CsGeI_2Br$ and $FASnI_3$ can play a significant role. Tin (Sn) and germanium (Ge) based materials can be promising substitutes for lead (Pb) based materials in the development of Perovskite solar cells (PSC) due to their superior optical properties, higher carrier mobility, and better performance. This research aims to enhance the efficiency of $CsGeI_2Br/FASnI_3$ double absorber-based (PSC), where PCBM was used as the ETL and PTAA as the HTL. The analysis was conducted by varying the absorber layer's thickness, doping density, and defect density using the SCAPS-1D numerical simulator and investigating the influence on key performance parameters such as power conversion efficiency (PCE), short circuit current density (J_{sc}), open circuit voltage (V_{oc}) and fill factor (FF). Before optimization the device structure (FTO/PCBM/$CsGeI_2Br$/$FASnI_3$/PTAA/Au) provide a PCE of 21.20%, J_{sc} of 28.70 (mA/cm^2), V_{oc} of 1.16 V and FF of 63.63% but after considering the standard optimized parameters the device achieved a PCE of 35.00%, J_{sc} of 30.44 (mA/cm^2), V_{oc} of 1.30 V and FF of 88.46%. Additionally, to evaluate the optimized device's reliability and stability, the following analyses are performed: temperature (T), series resistance (R_s), and shunt resistance (R_{sh}). The simulation outcomes were validated through comparison with prior research. The proposed device structure not only achieved superior performance but is also lead-free and cost-effective. The results demonstrate the potential of lead-free Sn /Ge-based perovskite architectures for high-performance and environmentally preferable photovoltaic applications**

***Index Terms*—Perovskite Solar Cell, SCAPS-1D Simulation, $CsGeI_2Br/FASnI_3$ Heterostructure, Organic Transport Layers, High Efficiency, Eco-Friendly Approach**

Md Abid Morshed is a master's student at the Department of Electrical and Electronic Engineering, American International University-Bangladesh (AIUB), Dhaka, Bangladesh. E-mail: 24-93482-2@student.aiub.edu

Mohammad Abdul Mannan serves as a Professor and Associate Dean of the Faculty of Engineering, American International University-Bangladesh (AIUB), Dhaka, Bangladesh. E-mail: mdmannan@aiub.edu

Md. Rifat Hazari serves as an Associate Professor and Special Assistant of the Department of EEE, American International University-Bangladesh (AIUB), Dhaka, Bangladesh. E-mail: rifat@aiub.edu

I. Introduction

THE 21st century has witnessed a substantial increase in global energy demand for driving the digital civilization and industrial economy [1], [2]. Currently, global energy consumption stands at approximately 29,471 TWh and is predicted to exceed 36,000 TWh by 2030 [3]. The majority of the demand is fulfilled by burning traditional fossil fuels. Whereas, these resources are finite, and overutilization can worsen global warming by increasing greenhouse gas emissions [4]. Consequently, it is urgent to migrate towards renewable energy sources, as they offer an environmentally friendly, cost-effective solution. Additionally, it can reduce dependence on finite energy sources and ensure long-term security [5].

Among various renewable energy sources, solar energy emerges as a prime candidate for replacing traditional fossil fuels due to its remarkable abundance, sustainability, and inexhaustibility [6]. Solar energy is readily available worldwide, making it more viable for real-world applications. Photovoltaic technology offers clean, sustainable solutions by converting solar irradiance directly into electricity [7], [8]. In the field of photovoltaics, PSC offers a revolutionary third-generation technology with exceptional optoelectronic properties, including higher absorption, longer diffusion length, tunable bandgap, and low-cost fabrication [9]. Perovskite material utilizes ABX_3 crystal structure, where A and B are cations, and X is a halide anion [10]. However, single-junction PSCs are limited by the Shockley-Queisser limit. To overcome this limitation and harness a wide spectrum, a tandem solar cell is proposed. which can utilize multiple active layers with different band gaps to collect both high and low energy photons [11]. The commercialization of PSCs is hindered by the presence of toxic lead (Pb), posing environmental and health risks [12]. If lead (Pb) can be replaced by eco-friendly alternatives with the same optical properties, it can be a promising solution.

In a recent study, the author explored the $FASnBr_3$ absorber with ETL (PCBM) and investigated the impact of thickness and temperature variation. Additionally, highlight the importance of band alignment between the ETL/absorber for reducing non-radiative recombination [13]. On the other hand, another author utilized $FASnI_3$ as the bottom active layer and focused on increasing light absorption by varying the cell thickness. Finally, they achieved a total PCE of 28.22%, J_{sc} of 27.886

(mA/cm^2), V_{oc} of 1.14 V, and FF of 88.74% [14]. A similar investigation was conducted by another author in a single junction structure using $FASnI_3$ as an absorber layer, after systematically varying thickness, doping, bandgap, and electron affinity, achieving a PCE of 14.17% [15]. Following this approach, another study explores an $FAGeI_3$ absorber with an organic HTL (PTAA) and proposes a lead-(Pb)- free device structure. After optimizing the thickness of ETL and HTL, a PCE of 15.62% was achieved [16]. However, another author reported a $CsGeI_2Br$ absorber-based single-junction structure in which ZnO is the most suitable HTL. After optimizing different parameters, the final outcome achieved a PCE of 29.37% [17]. Unlike earlier, the author analyzes a lead (Pb)- based $CsPbI_3/MoSe_2$ double absorber structure with a theoretical efficiency of 41.86%. To achieve this remarkable efficiency, the researcher adjusted the defect density and thickness of both active layers. Additionally, the impact of series resistance and temperature on device performance was evaluated [18]. However, lead (Pb)-based structures offer superior efficiency; we have to avoid them due to their toxicity and environmental risks [19].

In this proposed study, a numerical simulation was conducted using SCAPS-1D. PCBM and PTAA are used as the organic ETL and HTL, respectively, and gold (Au) as the back contact. Additionally, $CsGeI_2Br$ functions as the top layer, $FASnI_3$ acts as the bottom layer. By utilizing tin (Sn) and germanium (Ge)-based structures instead of lead (Pb), this research promotes green technology that maintains high efficiency and is ecologically sound. Therefore, the oxidation of tin (Sn^{2+} to Sn^{4+}) in $FASnI_3$ introduces deep trap states that act as carrier recombination centres, along with higher defect density and lower carrier mobility, which ultimately contribute to lower V_{oc}. In this study, experimentally reported degradation effects were incorporated into the SCAPS-1D simulation by using experimentally realistic defect densities to account for non-radiative recombination losses. On the other hand, Ge-based active layers exhibit better stability, lower defect density, and higher carrier mobility [20]. Finally, after optimizing specific parameters, the device achieved PCE = 35.0%, FF = 88.46%, J_{sc}= 30.44 (mA/cm^2) and V_{oc} = 1.30 V. The overall performance of the proposed PSC represents a remarkable achievement in photovoltaic research, ensuring lead-free, low-cost fabrication and sustainability.

II. Device Structure

In this analysis, a multi-junction PSC is proposed. $CsGeI_2Br$ is utilized as the top layer, and $FASnI_3$ is used as the bottom layer. Two different bandgap active layers expedited the collection of a broad solar spectrum. Both absorbers perform more effectively by using tin (Sn) and germanium (Ge) instead of lead (Pb). The top absorber $CsGeI_2Br$ exhibits superior thermal and moisture stability, and the bottom absorber $FASnI_3$ improves structure integrity [13]. Fig. 1 displayed a double absorber-based PSC (FTO/PCBM /$CsGeI_2Br$/ $FASnI_3$/PTAA /Au) structure. Where FTO is used as the front contact and gold (Au) serves as the back contact. The organic materials PCBM and PTAA are employed as the electron transport layer (ETL) and hole transport layer (HTL), respectively. PCBM demonstrates favorable conduction-band alignment with $CsGeI_2Br$ ($\Delta EC = -0.14$ eV), facilitating efficient electron extraction. Similarly, PTAA achieves a near-flat valence-band offset with $FASnI_3$ ($\Delta EV = -0.13$ eV), which enhances hole extraction and reduces interfacial recombination. These advantageous band alignments justify the selection of PCBM and PTAA over alternative charge transport layers, including ZnO, CuSCN, and P_3HT. Additionally, they are lightweight, flexible, and suitable for low-cost fabrication. Therefore, the entire simulation was conducted at 300 K with an AM 1.5 G light spectrum and a 1×10^6 Hz frequency. Table I shows interfacial layers (PCBM/$CsGeI_2Br$ and $FASnI_3$/PTAA) for enhancing electric field, stability, and reduced recombination. The ideal interface defect parameters were intentionally adopted to isolate bulk absorber behavior. Consequently, the simulated V_{oc} and FF should be regarded as upper-bound values. However, the initial parameters used in this study are collected from previous literature in Table II and Table III displays various properties of proposed solar cell before optimization.

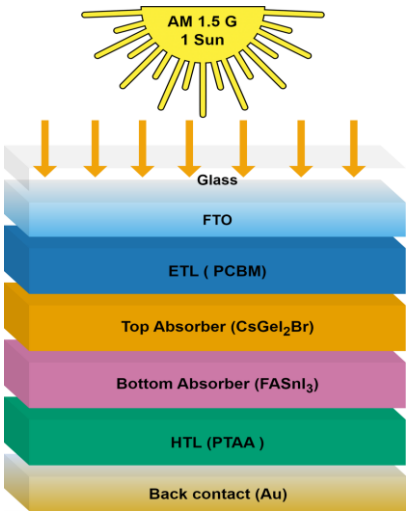

Fig. 1. Device Structure of $CsGeI_2Br$ and $FASnI_3$ based double absorber PSCs

A. *Energy band profile*

In perovskite solar cells, appropriate band alignment between the absorber and charge transport layers (ETL/HTL) is essential for efficient charge extraction and reduced interfacial recombination [21]. The conduction band offset (CBO) at the PCBM/$CsGeI_2Br$ interface and the valence band offset (VBO) at the $FASnI_3$/PTAA interface are primarily determined by the electron affinity (χ) and bandgap (E_g) values of the constituent materials. The CBO is defined as $\Delta EC = (\chi_{abs} - \chi_{ETL})$ = (3.76-3.90) = - 0.14eV [22]. A positive CBO forms a spike-like band alignment, while a negative CBO forms a cliff-like alignment. In general, a moderate positive CBO can suppress interfacial recombination by creating an energy barrier for minority carriers, thereby improving V_{oc}. However, an excessively large spike may impede electron transport. In contrast, a negative CBO (cliff) generally promotes interfacial recombination and may reduce V_{oc} and overall device efficiency. Similarly, the VBO is defined as $\Delta EV = (\chi_{abs} + E_{g,abs}) - (\chi_{HTL} - E_{g,HTL})$ = (3.72+1.41) - (2.3+2.96) = - 0.13eV [22]. An appropriate positive VBO can facilitate hole extraction while suppressing interfacial recombination. However, an excessively large VBO

may create a transport barrier for holes, weaken carrier extraction, and increase recombination losses. Therefore, proper band alignment is crucial for minimizing carrier losses and achieving high photovoltaic performance. Fig. 2 defines the band alignment profile for the proposed device structure. The diagram illustrates how the device materials contact each other. where E_v represents the valence band, and E_c defines the conduction band. Similarly, F_p shows the Fermi level for the p-type region, and F_n represents the Fermi level for the n-type region.

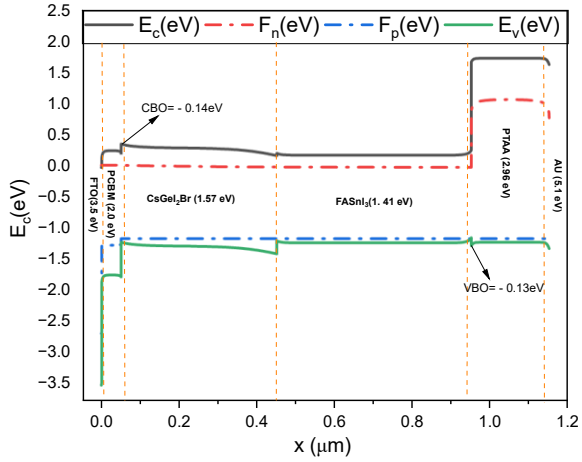

Fig. 2. Band alignment diagram of dual-absorber (PSCs).

III. Simulation Methods

This study focuses on numerical simulation and the optimization of device structure. There are several software programs for analyzing and optimizing different performance parameters of a solar cell, but SCAPS-1D is the most prominent. Because the observation is closely matched with the experimental result when defect and parasitic resistance are considered [23]. Additionally, it aligns with previously reported research, as most researchers have suggested. The software is developed by Prof. Mark Burgelman, University of Gent [24]. The one-dimensional software supports up to seven material layers, including p-n-type semiconductors. It can evaluate the effects of defects, doping, thickness, temperature, resistance, and capacitance on various solar cell parameters. The software allows control of various parameters that affect device functionality. However, it has some limitations that can lead to differences in experimental results. The software is based on one-dimensional Poisson and continuity equations to model and analyze the semiconductor material [8]. Equation 1: defines the poisson equation.

$$\frac{d^2\psi}{dx^2} = -\frac{q}{\epsilon}(p - n + N_D^+ - N_A^-) \quad (1)$$

Here, ψ denotes electrostatic potential, q denotes the charge, and N_D^+ and N_A^- represent the donor and acceptor concentrations. Whereas ϵ is a dielectric constant. Finally, n and p denote electron and hole concentration [25]. The continuity equations are represented by equations 2 and 3.

$$\frac{d_n}{d_t} = -\frac{1}{q}\frac{dJ_n}{dx} + (G_n - R_n) \quad (2)$$

$$\frac{d_p}{d_t} = -\frac{1}{q}\frac{dJ_p}{dx} + (G_P - R_p) \quad (3)$$

Where G_n and G_p are the generation rates, J_n and J_p are the current densities, and R_n and R_p represent the recombination rates of electrons and holes, respectively [25]. Equations 4 and 5 are used to calculate carrier current densities in the PSC [16].

$$J_n = qn\mu_n \in +qD_n\partial_n \quad (4)$$

$$J_p = qp\mu_p \in +qD_p\partial_p \quad (5)$$

In this context, μ_n and μ_p represent electron and hole mobilities, respectively, while D_n and D_p denote their diffusion coefficients . Equation 6 is used to calculate the FF of a solar cell and equation 7 represents the PCE of a solar cell, with respect to input power [23].

$$FF = \frac{V_{mp} \times J_{mp}}{V_{oc} \times J_{sc}} \quad (6)$$

$$PCE = \frac{V_{oc} \times FF \times J_{sc}}{P_{in}} \quad (7)$$

The maximum obtained voltage and current are denoted by V_{mp} and J_{mp}, respectively. P_{in} defines the input power [23].

TABLE I
Interface Defect Properties of the Proposed Dual-Absorber PSC

Parameter	PCBM \ $CsGeI_2Br$	$FASnI_3$ \ PTAA
Type of defect	Neutral	Neutral
Capture cross-section (cm^2)	1.00×10^{-19}	1.00×10^{-19}
State distribution	Single	Single
Energy level E_t	Above highest Ev	Above highest Ev
Reference Energy E_r (eV)	0.600	0.600
Total density ($1/cm^3$)	1.00×10^{10}	1.00×10^{10}

TABLE II
Material Parameters of the Proposed Solar Cell

Parameters	ETL	Absorber		HTL	TCO
	PCBM [26]	$CsGeI_2Br$ [27]	$FASnI_3$ [14]	PTAA [28]	FTO [5]
W_{th} (μm)	0.05	0.40*	0.50*	0.2	0.001
E_g (eV)	2.0	1.579	1.41	2.96	3.5
χ_e (eV)	3.9	3.76	3.72	2.3	4.0
ε_r	3.9	18.0	8.2	9.0	9.0
N_{CB},($1/cm^3$)	2.50E+21	9.65E+17	1.0E+18	2.0E+18	2.2E+18

N_{VB},(1/cm^3)	2.50E+21	1.04E+18	1.0E+18	1.0E+19	1.8E+19
$V_{te,}$ & V_{th} (cm/s)	1.0E+7	1.0E+7	1.0E+7	1.0E+7	1.0E+7
μ_e (cm^2/Vs)	2.0E-1	2.0E+1	2.2	1.0	2.0E+1
μ_h (cm^2/Vs)	2.0E-1	2.0E+1	2.2	4.0E+1	1.0E+1
N_D (1/cm^3)	2.93E+17	-	-	-	2.0E+19
N_A (1/cm^3)	-	1.0E+16	7.0E+16*	1.0E+18	-
N_t (1/cm^3)	1.0E+15	1.0E+14	1.0E+15*	1.0E+15	1.0E+15

[a.] *Parameters were varied in this study using the SCAPS-1D

TABLE III
PHOTOVOLTAIC PROPERTIES OF THE SOLAR CELL BEFORE OPTIMIZATION

Different configuration	**FF (%)**	**V_{oc} (Volts)**	**J_{sc} (mA/cm^2)**	**PCE (%)**
FTO/PCBM/$CsGeI_2Br$/ $FASnI_3$/PTAA/Au	63.63	1.1605	28.70	21.20

IV. RESULT & DISCUSSION

A. Effects of bottom absorber thickness on (J_{sc}, V_{oc}, PCE and FF) of the PSCs.

The absorber layer represents the most sensitive and primary segment of a photovoltaic device structure. The main responsibility of an absorber layer is to capture solar photons and convert them into electricity. It directly influences absorption and energy conversion capability [8], [15]. A well-optimized absorber layer can minimize manufacturing cost and ensure cell lifetime.

Moreover, a well-optimized thickness can regulate internal and shunt resistances [29]. If the thickness is too thick, it increases recombination at the contact side and reduces the carrier lifetime, resulting in a voltage drop. As a result, researchers suggested maintaining a thickness range of 0.5-1.5 µm [30]. The investigation is performed on the bottom absorber layer ($FASnI_3$) with a thickness range of 0.05 µm to 2 µm, with PCBM as the ETL, PTAA as the HTL, and gold (Au) as the back contact; other device parameters remain unchanged.

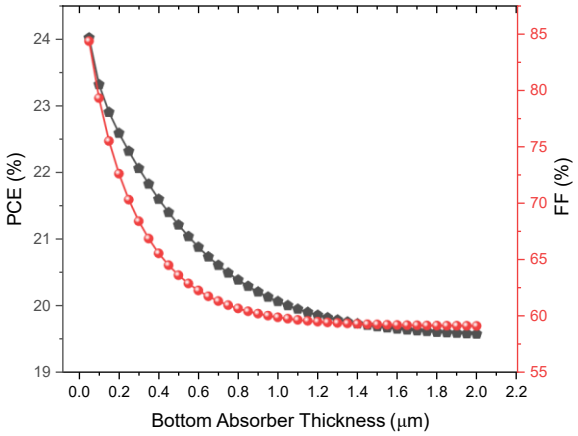

Fig. 3. Impact of ($FASnI_3$) bottom absorber thickness variation on PCE and FF

Fig. 3 shows the relationship of FF and PCE with bottom absorber thickness; both parameters decrease with increasing thickness. The maximum PCE = 24% is obtained at the thickness of 0.05 µm, and the minimum PCE = 19.58% is found at the thickness of 2 µm. Whereas, the maximum FF = 84.30% is found for a thickness of 0.05 µm, and the minimum FF = 59.14% is obtained for a thickness of 2 µm. A greater thickness absorbs more light and increases the recombination rate; as a result, it is associated with increased series resistance, carrier losses, and bulk recombination, which eventually decrease PCE and FF [9], [31]. Fig. 4 displays the relationship between V_{oc} and J_{sc} as a function of bottom absorber thickness. Where V_{oc} decreases, and J_{sc} increases at a given thickness. The maximum V_{oc} = 1.21 V is found at the thickness of 0.05 µm, and the minimum V_{oc} = 1.1539 V is obtained at the thickness of 2 µm. Moreover, the highest J_{sc} = 29.0 (mA/cm^2) is observed at a thickness of 0.75 µm, and the lowest J_{sc} = 23.51 (mA/cm^2) is observed at a thickness of 0.05 µm. The highest thickness allows more light to be absorbed and generates more carriers. As a result, J_{sc} increases at some point, but V_{oc} decreases. A thicker layer enhances recombination, increasing the dark saturation current and requiring carriers to travel a longer distance toward the contact [32]. Therefore, for further analyses, the selected thickness of the bottom absorber is set to 0.9 µm, even though a lower thickness yields better PCE. The value is taken as optimal to reduces fabrication complexity and maintain experimentally valid parameters because it strikes a critical balance between optical absorption capacity, charge transport kinetics, and practical manufacturing constraints [33], [9].

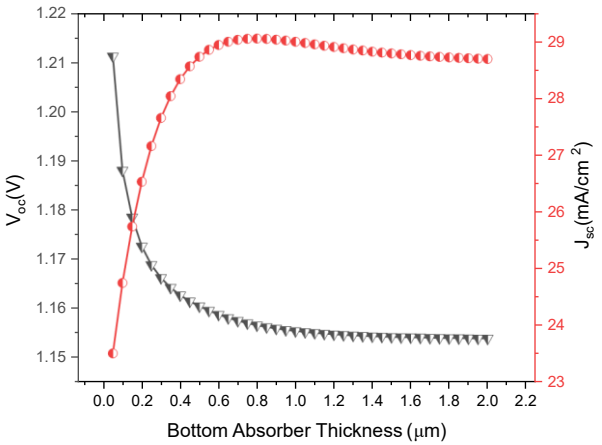

Fig. 4. Impact of ($FASnI_3$) bottom absorber thickness variation on J_{sc} and V_{oc}

B. Effects of bottom absorber acceptor density (N_A) on (J_{sc}, V_{oc}, PCE and FF) of the PSCs.

The main responsibility of acceptor density (N_A) is to regulate hole concentration in p-type material. Tuning N_A is vital because a minimal amount of dopant can significantly boost overall performance [34]. The limited range of N_A can enhance the electric field at the p-n junction. This improved

band alignment at the junction and enhanced hole extraction to the transport layer, but excessive N_A creates coulomb traps that reduce hole mobility and introduce unwanted sheet resistance [8]. The investigation is performed on the bottom absorber layer ($FASnI_3$) over a doping density range of 1.0E+13 ($1/cm^3$) to 1.0E+20 ($1/cm^3$), with PCBM and PTAA used as the ETL and HTL, respectively. Additionally, gold (Au) is used as the back contact, and other device parameters remain constant. Fig. 5 represents the relationship between PCE and FF with doping density (N_A). Both of the parameters increase with doping density. The maximum PCE = 33.53% is found at the doping density of 1.0E+20 ($1/cm^3$), and the minimum PCE = 15.29% is obtained for the doping density of 1.0E+13 ($1/cm^3$). Moreover, the maximum FF = 88.60% is observed for a doping density of 1.0E+20 ($1/cm^3$). whereas, the minimum FF = 47.76% acquired at the doping density of 1.0E+13 ($1/cm^3$). Higher N_A increases PCE and FF at a certain point because it reduces resistivity and minimizes series resistance, but excessive N_A introduces auger recombination, which shortens the carrier lifetime and eventually decreases PCE and FF [35].

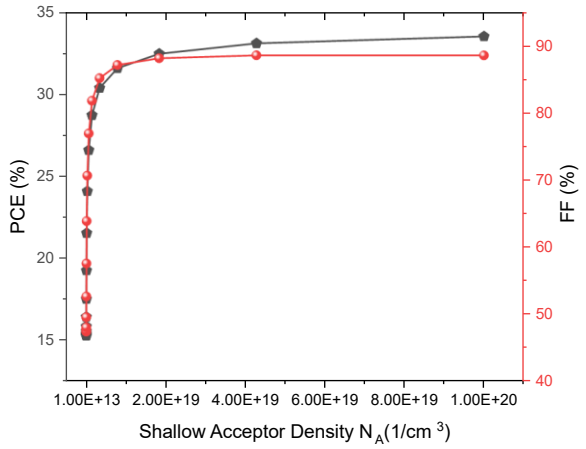

Fig. 5. Impact of ($FASnI_3$) bottom absorber doping density variation on PCE and FF

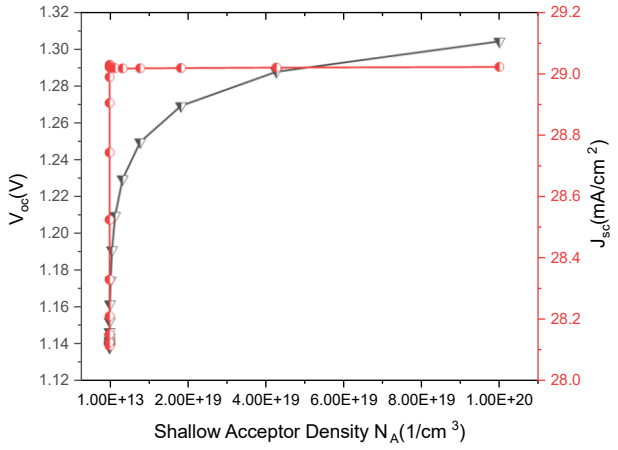

Fig. 6. Impact of ($FASnI_3$) bottom absorber doping density variation on J_{sc} and V_{oc}

Fig. 6 displays the relationship between V_{oc} and J_{sc} with doping density. V_{oc} increases significantly, and J_{sc} increases slightly with doping density. The maximum V_{oc} = 1.30 V is found for the doping density of 1.0E+20 ($1/cm^3$), and the minimum V_{oc} = 1.14 V is obtained at the doping density of 1.0E+13 ($1/cm^3$). Higher doping increases the hole Fermi energy, thereby increasing the built-in potential; as a result, V_{oc} increases with higher N_A [29]. Moreover, the maximum J_{sc} = 29.0 (mA/cm^2) is found for the doping density of 1.0E+20 ($1/cm^3$) and the minimum J_{sc} = 28.12 (mA/cm^2) is obtained at the doping density of 1.0E+13 ($1/cm^3$). Higher doping increases the likelihood of carrier recombination, which results in hindering carrier mobility and carrier collection; that's the reason J_{sc} slightly increases or remains constant at higher N_A [30]. However, experimentally reported Sn-based perovskite films generally exhibit background hole concentrations in the range of approximately 1.0E+15 to 1.0E+18 ($1/cm^3$) due to the oxidation of Sn^{2+} to Sn^{4+}, while bulk defect densities commonly remain around 1.0E+15 to 1.0E+16 ($1/cm^3$) depending on fabrication methods [36]. Within the experimentally reported doping-density range of 1.62E+15 ($1/cm^3$) to 1.0E+18 ($1/cm^3$), the the proposed device exhibits a PCE increase from 15.56% to 28.73%, while V_{oc}, J_{sc} and FF improve by 0.07 V, 0.10 (mA/cm^2) and 34.37% , demonstrating that doping density remains a dominant limiting factor under practical conditions. Therefore, for further analysis, the optimal doping density is taken as 1.0E+19 ($1/cm^3$). The optimized parameters used in this study should be interpreted as representing a best-case material quality rather than the average experimental condition.

C. Effects of bottom absorber defect density (N_t) on (J_{sc}, V_{oc}, PCE and FF) of the PSCs.

Total defect density (N_t) governs charge-carrier dynamics in solar cells and is inversely related to carrier lifetime; higher N_t leads to reduced cell lifetime [37]. Proper tuning of N_t is crucial to suppress Shockley–Read–Hall (SRH) non-radiative recombination and minimize energy losses, which is described by Equation 8.

$$R_{SRH} = \frac{n_p - n_i^2}{\tau_p(n+n_1)+\tau_n(p+p_1)} \quad (8)$$

Here, p and n represent hole/electron concentration. Whereas, p_1 and n_1 define electron/hole concentration according to trap energy level. In addition, τ_n and τ_p indicates lifetime of electron/hole. Finally, n_i define intrinsic carrier density [38].

Additionally, tuning N_t also helps researchers identify the most sensitive region of the device, where defect density primarily impacts efficiency [39]. Usually, a higher defect density reduces the internal electric field, hindering photon absorption and increasing resistance, thereby lowering performance [40]. For that reason, defect concentration of 1.0E+14 ($1/cm^3$) or lower is suggested for good performance [10]. This analysis is performed on the bottom active layer ($FASnI_3$) across a defect density range of 1.0E+13 ($1/cm^3$) to 1.0E+17 ($1/cm^3$), where PCBM and PTAA are utilized as the ETL and HTL, respectively, and Au is used as the back contact; other device parameters remain constant. Fig. 7 represents the relationship between PCE and FF with total defect density. Both parameters decrease sharply with increasing defect density. The maximum PCE = 35.80% is found for the defect density of 1.0E+13 ($1/cm^3$), and the minimum PCE = 23.0% is obtained at the defect density of 1.0E+ 17 ($1/cm^3$). Moreover, the maximum FF = 87.83% is observed at a defect density of

1.0E+13 (1/cm^3), and the minimum FF = 80.76% is observed at a defect density of 1.0E+17 (1/cm^3). Higher defect density increases internal series resistance and hinders synchronized charge extraction; as a result, PCE and FF decrease [41]. Fig. 8 illustrates the relationship between V_{oc} and J_{sc} with total defect density. Both parameters decrease with increasing defect density. The maximum V_{oc} = 1.33 V is found for the defect density of 1.0E+13 (1/cm^3), and the minimum V_{oc} = 1.19 V is found at the defect density of 1.0E+17 (1/cm^3). Moreover, the highest J_{sc} = 30.68 (mA/cm^2) is acquired at a defect density of 1.0E+13 (1/cm^3), and the minimum J_{sc} = 23.91 (mA/cm^2) is found at a defect density of 1.0E+17 (1/cm^3). Higher defect density introduces (SRH) recombination, which is responsible for dark saturation current and shorter carrier lifetime, that eventually lowering V_{oc} and J_{sc} [23]. Therefore, across the experimental defect density range around 1.0E+15 (1/cm^3) to 1.44E+16 (1/cm^3), the PCE decreases from 29.27% to 25.74%, while V_{oc}, J_{sc}, and FF decline by 0.05 V, 3.45 (mA/cm²), and 3.34%, respectively, demonstrating the critical role of doping concentration in practical device performance. For the next analysis the optimal defect density is taken as 1.0E+14 (1/cm^3). The optimized parameters adopted in this study represent an idealized best-case material quality rather than typical experimental conditions.

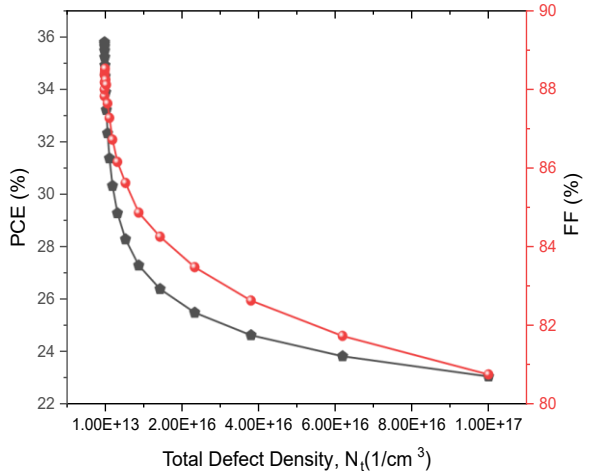

Fig. 7. Impact of ($FASnI_3$) bottom absorber defect density variation on PCE and FF

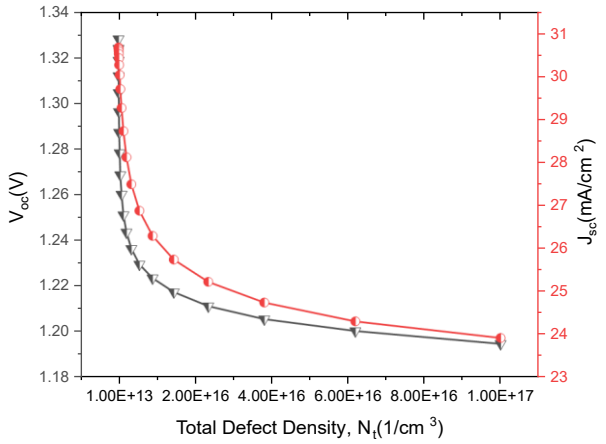

Fig. 8. Impact of ($FASnI_3$) bottom absorber defect density variation on J_{sc} and V_{oc}

D. Effects of top absorber thickness on (J_{sc}, V_{oc}, PCE and FF) of the PSCs.

The thickness of the $CsGeI_2Br$ top absorber was optimized to maximize the photovoltaic performance of the proposed device. In this analysis, the top absorber ($CsGeI_2Br$) thickness ranged from 0.05 µm to 2 µm, with PCBM and PTAA used as ETL and HTL, and gold (Au) as the back contact; other device parameters remained at optimal values. Fig. 9 shows the relationship of PCE and FF with top absorber thickness; both parameters show a slight downward trend with increasing thickness. The maximum PCE = 35.0% is obtained at the thickness of 0.05 µm, and the minimum PCE = 34.07 % is found at the thickness of 2 µm. Whereas the maximum FF = 89% is found for a thickness of 0.05 µm, and the minimum FF = 87.95% is obtained for a thickness of 2 µm. Fig. 10 displays the relationship of V_{oc} and J_{sc} with top absorber thickness. V_{oc} decreases drastically, and J_{sc} increases at a certain point with thickness. The maximum V_{oc} = 1.31 V is obtained at the thickness of 0.05 µm, and the minimum V_{oc} = 1.27 V is found at the thickness of 2 µm. Moreover, the highest J_{sc} = 30.52 (mA/cm^2) is found at a thickness of 1.0 µm, and the lowest J_{sc} = 30.40 (mA/cm^2) is observed at a thickness of 2.0 µm. However, the selected thickness of the top absorber is set to 0.35 µm for further analyses.

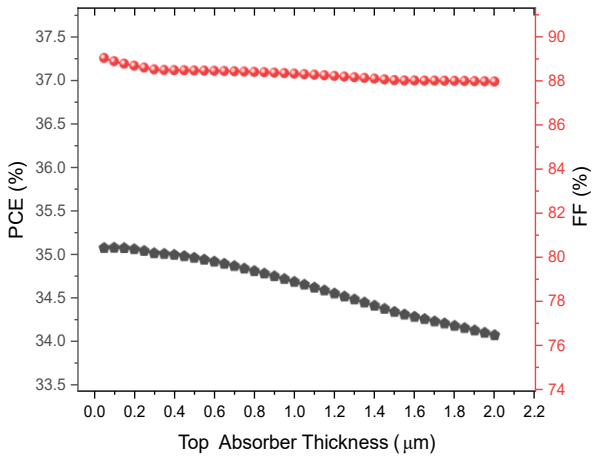

Fig. 9. Impact of ($CsGeI_2Br$) top absorber thickness variation on PCE and FF

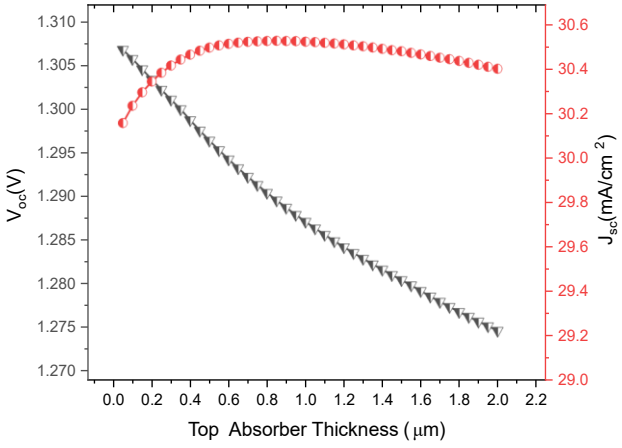

Fig. 10. Impact of ($CsGeI_2Br$) top absorber thickness variation on J_{sc} and V_{oc}

V. Optimized Device Performance Analysis

A. Device Stability and Performance Sensitivity Analysis

The $CsGeI_2Br/FASnI_3$ dual-absorber perovskite solar cell (PSC) partially enhances device stability through halide mixing and the use of thermally stable, all-inorganic $CsGeI_2Br$ as the top absorber. However, the stability of tin- and germanium-based perovskites is limited by the oxidation of Sn^{2+} to Sn^{4+} and Ge^{2+} to Ge^{4+} upon exposure to oxygen, a consequence of their lower redox potentials relative to lead-based counterparts [42]. This oxidation generates metal vacancies and induces self-p-type doping, which increases non-radiative recombination, reduces carrier mobility and shunt resistance, and accelerates device degradation [43]. The incorporation of bromine and cesium doping mitigates these degradation mechanisms by suppressing oxidation, enhancing defect tolerance, and improving lattice and crystal stability [4]. Furthermore, the dual-absorber configuration reduces thermalization losses, thereby contributing to improved operational stability.

B. Effects of temperature on the proposed PSCs.

Solar panels are installed outdoors and operate in shifting weather conditions. When solar radiation strikes panels, it significantly increases panel temperature and affects several physical parameters [44]. So, it is important to understand the temperature dependence of a solar cell to evaluate real-world performance and stability. Moreover, high temperature can trigger structural changes, create interfacial defects, and induce phase transitions. This phenomenon must be considered to improve material engineering and stable performance [45]. For this analysis, the temperature varied from 280 K to 400 K while keeping all other parameters at optimized values. Fig. 12 shows the influence of temperature on device performance parameters V_{oc} and J_{sc}. Where V_{oc} shows a downward trend, and J_{sc} displays a stable trend. The decline in V_{oc} is caused by the rise in J_o. As the temperature rises, J_o increases exponentially, leading to greater recombination and a higher intrinsic carrier concentration. So, V_{oc} declines according to the diode equation 9:

$$V_{oc} = \frac{KT}{q} \ln\left[\frac{Jsc}{J_o} + 1\right] \tag{9}$$

Where T is the absolute temperature, K is the Boltzmann constant, J_o is the dark saturation current, q is the elementary charge [46], [17].

From Fig. 12, the maximum V_{oc} = 1.31 V was observed at the lowest temperature of 280K, and the lowest V_{oc} = 1.18 V was observed at the highest temperature of 400K. Moreover, the J_{sc} shows a slight upward trend from 30.447 (mA/cm^2) to 30.52 (mA/cm^2) at 280K and 400K. Fig. 11 evaluates the influence of temperature on the performance parameters PCE and FF. Both of which show a downward trend with temperature increase. The maximum PCE = 35.54% is observed at 280K, and the minimum PCE = 30.89% is observed at 400K. Additionally, the maximum FF = 88.82 % is observed at the lowest temperature of 280 K, and the minimum FF = 85.70 % is observed at the highest temperature of 400 K. Higher temperatures reduce carrier mobility through phonon scattering, while the decline in PCE and FF is mainly caused by the exponential rise in J_0, leading to increased non-radiative recombination [47].

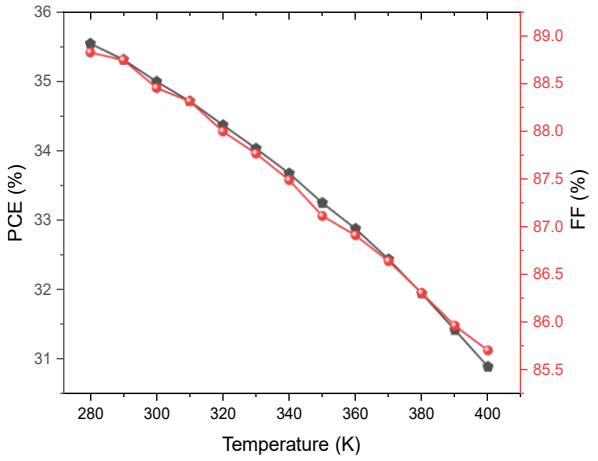

Fig. 11. Impact of temperature on PCE and FF

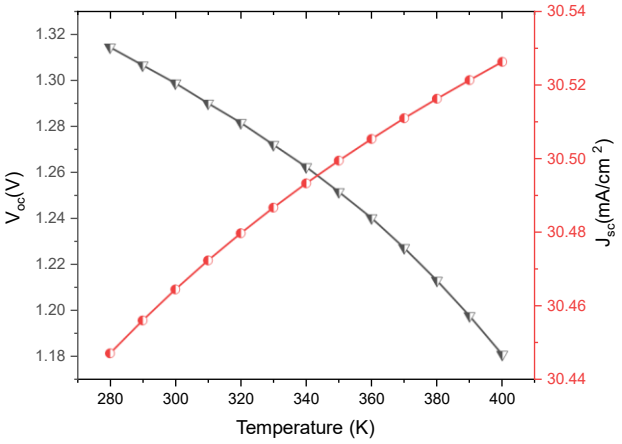

Fig. 12. Impact of temperature on J_{sc} and V_{oc}

C. Effects of series resistance (R_s) on the proposed PSCs.

The performance of a solar cell is strongly influenced by the series resistance (R_s), which is also known as the parasitic resistance. To maximize solar cell performance, it is ideal to maintain R_s at zero, but in practice this doesn't happen [4]. In practice, R_s arises from the metallic contacts at FTO/ETL, ETL/absorber, absorber/HTL, and the back contact. R_s is the sum of all resistance due to metallic contact and ohmic contact of semiconductor material [48]. Moreover, R_s plays a critical role in influencing FF and PCE, but V_{oc} and J_{sc} remain constant with R_s but extremely higher R_s can degrade J_{sc} [26]. The Shockley equation 10 gives a relationship between current - voltage (J-V) and R_s of the solar cell :

$$J_{sc} = J_p - J_o exp\left[\frac{q_e(V+IR_S)}{\eta kT}\right] \tag{10}$$

Where J_p represents the photocurrent density, V_o is the output voltage, and J_o is the dark saturation current. Finally, n represents the diode ideality factor [48].

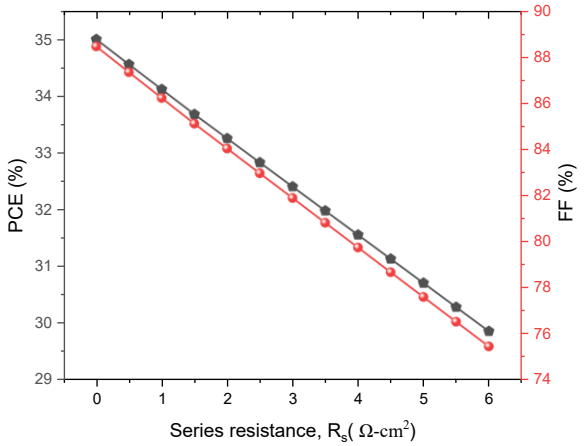

Fig. 13. Impact of series resistance on PCE and FF

The analysis is conducted using all optimized values, with the R_s varying from 0 Ω-cm^2 to 6 Ω-cm^2 and all other parameters remaining constant. Fig. 13 shows the effect of R_s on PCE and FF; both parameters decrease with R_s. The PCE shows a downtrend from 35.0% to 29.86%, and the FF shows a downtrend from 88.46% to 75.45% at R_s of 0 Ω-cm^2 and 6 Ω-cm^2. Higher series R_s reduces effective voltage and current tracking at the maximum power points, thereby degrading FF and PCE [49].

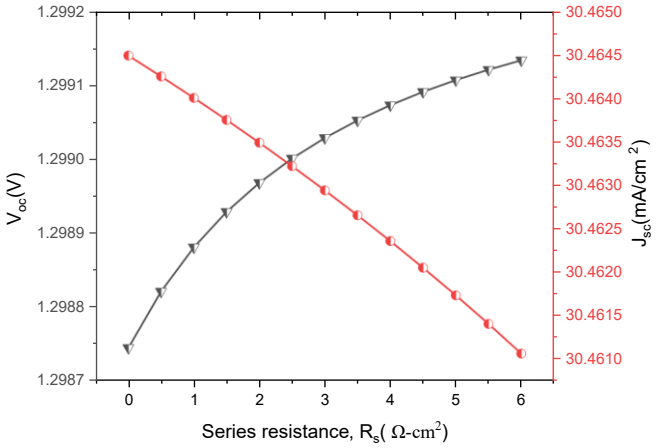

Fig. 14. Impact of series resistance on J_{sc} and V_{oc}

Fig. 14 displays the effect of series resistance (R_s) on J_{sc} and V_{oc}. Both parameters remain constant at different R_s. It is therefore concluded that the R_s variation doesn't affect J_{sc} and V_{oc}. The J_{sc} of 30.46 (mA/cm^2) and V_{oc} of 1.30 V were obtained over the range of R_s variation. As low R_s provide better performance, this can be achieved by doping optimization, surface passivation, and contact engineering [4].

D. Effects of shunt resistance (R_{sh}) on the proposed PSCs.

To maintain the maximum potentiality of a solar cell, it must maintain an infinite shunt resistance (R_{sh}), but in practice, it is not possible to maintain it at infinity. Because R_{sh} represents an undesired leakage pathway for photo-generated carriers that arises from factors such as pinholes in the active layer, fabrication flaws, crystallographic defects, grain boundaries, and the material itself [49]. As R_{sh} decreases, it significantly impacts V_{oc}, FF and PCE. The Shockley equation 11, 12 describes the influence of R_{sh} on current density - voltage (J-V) characteristics :

$$J_{sc} = J_p - J_o\left[exp\left(\frac{q_e(V+IR_S)}{\eta kT}\right) - 1\right] - \left(\frac{V+IR_S}{R_{sh}}\right) \quad (11)$$

$$V_{oc} = \left(\frac{\eta kT}{q_e}\right)\ln\left\{\frac{J_p}{J_o}\left(1 - \frac{V_{oc}}{J_p R_{sh}}\right)\right\} \quad (12)$$

Here, J_p represents photocurrent density, q_e describes the elementary charge, and J_o represents the dark saturation current. Whereas, R_s and R_{sh} denote series and shunt resistance, and K refers to the Boltzmann constant [26].

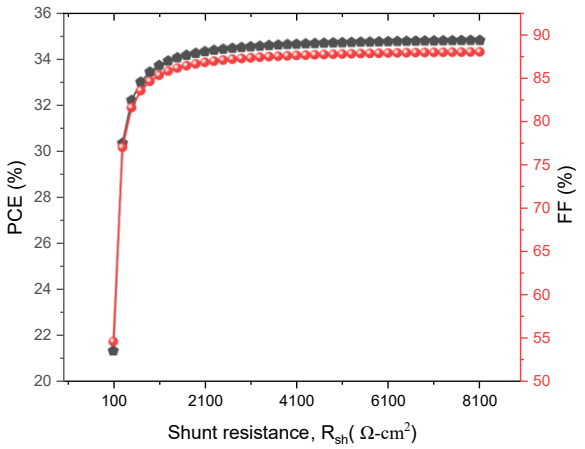

Fig. 15. Impact of shunt resistance on PCE and FF

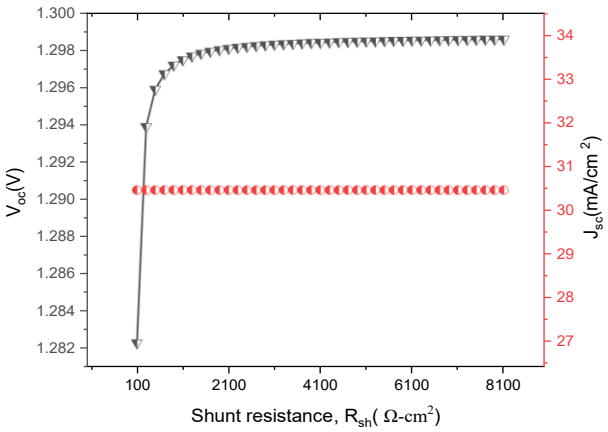

Fig. 16. Impact of shunt resistance on J_{sc} and V_{oc}

The investigation is conducted utilizing all optimized parameters, with shunt resistance varying from 100 Ω -cm^2 to 8100 Ω -cm^2 and all other parameters kept unchanged. Fig. 15 depicts the effect of R_{sh} on the PCE and FF, both of the parameters show an upward trend with R_{sh}, Where the maximum PCE = 34.83% is found at the R_{sh} of 8.1×10^3 Ω -cm^2 and the minimum PCE = 21.32% is obtained at the R_{sh} of 1×10^2 Ω -cm^2. Moreover, the maximum FF = 88.03% is found at the R_{sh} of 8.1×10^3 Ω -cm^2 and the minimum FF = 54.59% is obtained at the R_{sh} of 1×10^2 Ω -cm^2. Higher R_{sh} minimizes the leakage current near the maximum power point and allows the (J-V) curve to be more rectangular in shape [50]. Fig. 16

describes the effect of shunt resistance on V_{oc} and J_{sc}, where V_{oc} increases, and J_{sc} remains the same with R_{sh} increase. The highest V_{oc} = 1.30 V is found at R_{sh} of 8.1×10^3 Ω -cm^2 and the lowest V_{oc} = 1.28 V is obtained at the R_{sh} of 1×10^2 Ω -cm^2. Whereas, the J_{sc} = 30.46 (mA/cm^2) remains constant over the R_{sh} variation. Lower R_{sh} value weakens the Fermi level that leads to a decrease in V_{oc}, but J_{sc} only depends on the primary photon absorption, so it remains the same across the R_{sh} [51], [38]. However, it is observed that higher R_{sh} enhances PSC performance by minimizing recombination loss and leakage current. To maximize R_{sh}, pinhole-free film can be used by optimizing deposition conditions [52]. Finally, Table IV shows the overall performance of optimized PSC and Table V compares the proposed work with previously reported studies. The ($CsGeI_2Br/FASnI_3$) dual-absorber perovskite solar cell (PSC) achieves a simulated power conversion efficiency (PCE) of 35.0%. In contrast, the highest reported experimental $FASnI_3$ single-junction device attains approximately 10.8% [53]. As the device architectures differ, this comparison serves only as a reference to current experimental Sn-based PSCs. The elevated simulated efficiency is primarily attributed to idealized interface conditions, assumptions of low defect density and high doping levels, and the exclusion of Sn^{4+}-induced self-doping. Furthermore, the proposed dual-absorber $CsGeI_2Br$ /$FASnI_3$ device demonstrates a 5.63% higher PCE than the previously reported single-absorber $CsGeI_2Br$-based PSC [22]. Finally, this work achieved remarkable results compared with related work, and the outcome can significantly impact future third-generation photovoltaic research.

TABLE IV
OVERALL PERFORMANCE OF THE OPTIMIZED PSC

Different configuration	FF (%)	V_{oc} (Volts)	J_{sc} (mA/cm^2)	PCE (%)
FTO/PCBM/$CsGeI_2Br$/ $FASnI_3$/PTAA/Au	88.46	1.30	30.44	35.00

TABLE V
COMPARISON WITH PREVIOUSLY REPORTED STUDIES

Different configuration	FF (%)	V_{oc} (Volts)	J_{sc} (mA/cm^2)	PCE (%)	Work Type
FTO/TiO_2/n-$FA_{0.15}MA_{0.85}PbI_3$/p-$FA_{0.15}MA_{0.85}PbI_3$/Au	80.50	1.12	24.23	21.88	Experimental [54]
AI/BCP/C_{60}/$FASnI_3$/PREDOT:PSS/IOT	72.0	0.62	24.20	10.8	Experimental [53]
FTO/Pristine TiO_2/6% Target TiO_2/$FAPbI_3$/ Spiro-OMeTAD/Au	83.45	1.19	25.79	25.25	Experimental [55]
FTO/$CsGeI_2Br$/$CsGeI_3$/P3HT/Au	79.10	1.23	32.79	31.86	Simulated [56]
FTO/TiO_2/$CsGeI_2Br$/$CuSbS_2$/Pt	88.24	1.30	25.55	29.40	Simulated [27]
ITO/ZnSe/$FASnI_3$/CBTS/AU	78.01	1.36	29.39	31.29	Simulated [57]
FTO/TiO_2/$Cs_2AgBi_{0.75}Sb_{0.25}Br6$/$FASnI_3$/$Cu_2O$/Au	88.74	1.14	27.89	28.22	Simulated [14]
AI/ FTO/TiO_2/$FASnI_3$/CBTS/Au	83.20	1.12	29.61	26.67	Simulated [4]
FTO/TiO_2/n-$FASnI_3$/p-$FASnI_3$/CuSCN/Au	86.67	1.18	29.81	30.47	Simulated [58]
AI/SnO_2/$FASnI_3$/GO/Au	82.78	0.94	25.79	20.55	Simulated [59]
FTO/ZnO/$CsGeI_2Br$/CuSCN/Au	85.74	1.39	24.68	29.37	Simulated [17]
FTO/PCBM/$CsGeI_2Br$/ $FASnI_3$/PTAA/Au	88.46	1.30	30.44	35.00	**Proposed Work**

VI. CONCLUSION

In this study, a high-efficiency, low-cost, lead-free and sustainable photovoltaic device was proposed. The device is based on a $CsGeI_2Br/FASnI_3$ absorber layer, with the organic transport layers ETL (PCBM) and HTL (PTAA). After analyzing the influence of different parameters on device performance, namely PCE, J_{sc}, V_{oc} and FF. The selected top absorber thickness was 0.35 µm and the optimized parameters for the bottom absorber are a thickness of 0.9 µm, a doping density of 1.0E+19 (1/cm^3), and a defect density of 1.0E+14 (1/cm^3). After utilizing the optimal value, the proposed PSC exhibited a simulated PCE of 35.00%, J_{sc} of 30.44 (mA/cm^2), V_{oc} of 1.30V and FF of 88.46 %. The optimized device also includes temperature, series, and shunt resistance tests to evaluate environmental and parasitic-loss conditions. Additionally, the device represents a remarkable performance compared to previously published literature. To simplify the simulation, equal electron and hole mobilities were assumed. While experimental $FASnI_3$ generally demonstrates asymmetric carrier transport, this approximation is anticipated to have only a minor effect on the predicted device performance. Furthermore, the computational efficiency and environmentally sustainable approach of the device may facilitate advancements in third-generation photovoltaic research. Future investigations will incorporate experimentally

measured carrier mobilities and validate the proposed device through experimental fabrication.

Author contributions

Md. Abid Morshed carried out the main research work, including the simulation, data analysis, visualization, and preparation of the manuscript. Mohammad Abdul Mannan provided academic supervision, research guidance, idea generation and valuable feedback throughout the study and manuscript preparation. Md. Rifat Hazari provided external academic supervision, technical guidance, idea generation, data validation and constructive feedback on the research and manuscript.

REFERENCES

[1] A. Alsalme and H. Alsaeedi, "Twenty-Two Percent Efficient Pb-Free All-Perovskite Tandem Solar Cells Using SCAPS-1D," *Nanomaterials*, vol. 13, no. 1, p. 96, Dec. 2022, doi: 10.3390/nano13010096.

[2] M. Billah *et al.*, "Fuzzy Logic-Based LVRT Enhancement in Grid-Connected PV System for Sustainable Smart Grid Operation: A Unified Approach for DC-Link Voltage and Reactive Power Control," *Sustainability*, vol. 18, no. 5, p. 2448, Mar. 2026, doi: 10.3390/su18052448.

[3] K. K. Bharati, S. Yadav, V. P. Singh, R. Kumar, and P. Chaudhari, "Performance Optimization of Lead-Free $FASnI_3$ Perovskite Solar Cells with Optimized Absorber and Transport Layers," in *2025 IEEE 17th International Conference on Computational Intelligence and Communication Networks (CICN)*, Goa, India: IEEE, Dec. 2025, pp. 1663–1668. doi: 10.1109/CICN67655.2025.11368069.

[4] A. Yadav, A. Kumar, and S. M. Giripunje, "Photovoltaic performance optimization of CBTS based HTL integration in lead free perovskite solar cell: A SCAPS 1D simulation approach," *Micro and Nanostructures*, vol. 207, p. 208267, Nov. 2025, doi: 10.1016/j.micrna.2025.208267.

[5] E. L. Meyer, I. Vulindlela, A. Paca, M. A. Agoro, and N. Rono, "Numerical Simulation and Hole Transport Layers Optimization of a Lead Sulfide-Based Solar Cell with a Power Conversion Efficiency of Above 22%," *Coatings*, vol. 15, no. 3, p. 255, Feb. 2025, doi: 10.3390/coatings15030255.

[6] M. S. I. Ria *et al.*, "Exploring CaBCl3 (B K and Rb) chloroperovskites: DFT and SCAPS-1D insights into physical properties and solar cell performance," *Journal of Physics and Chemistry of Solids*, vol. 207, p. 112955, Dec. 2025, doi: 10.1016/j.jpcs.2025.112955.

[7] M. J. Rahman, Md. I. Ul Hoque, M. I. E. Jalal, U. Chowdhury, and U. M. Umama, "Investigation of varied Doping of ZnO as an ETL for $KSnI_3$ based Perovskite Solar Cell with ETL and Absorber Thickness Optimization," in *2025 International Conference on Electrical, Computer and Communication Engineering (ECCE)*, Chittagong, Bangladesh: IEEE, Feb. 2025, pp. 1–6. doi: 10.1109/ECCE64574.2025.11013548.

[8] Md. E. Ali, Md. M. Haque, and S. H. Cheragee, "Device modeling and numerical analysis of lead-free MASnI3/Ca3AsI3 based perovskite solar cells with over 38% efficiency," *Solar Energy*, vol. 288, p. 113309, Mar. 2025, doi: 10.1016/j.solener.2025.113309.

[9] M. A. Atem, B. Dridi Rezgui, I. Touhami, and M. Bouaïcha, "Numerical simulation and optimization of high-performance lead-based $FAMACsPb(IBr)_3$ perovskite solar cells using SCAPS 1D," *Results in Engineering*, vol. 29, p. 108555, Mar. 2026, doi: 10.1016/j.rineng.2025.108555.

[10] H.-J. Park, H. Son, and B.-S. Jeong, "SCAPS-1D Simulation for Device Optimization to Improve Efficiency in Lead-Free CsSnI3 Perovskite Solar Cells," *Inorganics*, vol. 12, no. 4, p. 123, Apr. 2024, doi: 10.3390/inorganics12040123.

[11] W. Akram, X. Li, S. Ahmed, Z. Ouyang, and G. Li, "A review of life cycle assessment and sustainability analysis of perovskite/Si tandem solar cells," *RSC Sustainability*, vol. 3, no. 1, pp. 21–36, 2025, doi: 10.1039/D4SU00431K.

[12] O. O. Moyofola and M. E. Emetere, "Numerical analysis of the optoelectronic properties of selected Sn-based perovskites solar cells using SCAPS simulation," *Results in Optics*, vol. 21, p. 100868, Dec. 2025, doi: 10.1016/j.rio.2025.100868.

[13] M. S. Nawaz Romel *et al.*, "Theoretical and device-level insights into FASnBr3 perovskite solar cells: a synergistic approach Combining density functional theory and SCAPS-1D," *Results in Physics*, vol. 82, p. 108593, Mar. 2026, doi: 10.1016/j.rinp.2026.108593.

[14] S. B. Almahsen and G. A. Al-Dahash, "High-efficiency lead-free all-perovskite tandem solar cells achieving 28.22 % power conversion efficiency: A Cs2AgBi0.75Sb0.25Br6/FASnI3 heterostructure design," *Results in Optics*, vol. 21, p. 100882, Dec. 2025, doi: 10.1016/j.rio.2025.100882.

[15] A. Shaikh, P. Hameed Shaikh, S. Ahmed Khatri, M. Saeed, H. Shah, and L. Kumar, "Performance Optimization in Lead-Free Perovskite Solar Cell: A Comparative Approach," *IEEE Access*, vol. 13, pp. 40747–40759, 2025, doi: 10.1109/ACCESS.2025.3543244.

[16] S. Ali, K. Ahmad, R. A. Khan, and P. Kumar, "Simulation-Based Studies on FAGeI3-Based Lead (Pb2+)-Free Perovskite Solar Cells," *Crystals*, vol. 15, no. 2, p. 135, Jan. 2025, doi: 10.3390/cryst15020135.

[17] S. Subba, A. Talukdar, J. Sarkar, and S. Chatterjee, "Investigations and optimizations of lead-free CsGeI 2 Br perovskite solar cell using numerical simulations and machine learning," *Journal of Physics and Chemistry of Solids*, vol. 209, p. 113281, Feb. 2026, doi: 10.1016/j.jpcs.2025.113281.

[18] G. Venkateswarlu and U. Nanda, "Highly Efficient Perovskite Heterojunction Solar Cell With Dual Absorber Layers for State of Art Photovoltaic Technologies," *IEEE Access*, vol. 13, pp. 62648–62659, 2025, doi: 10.1109/ACCESS.2025.3558867.

[19] Md. S. Rahman *et al.*, "Insights from computational analysis on novel Lead-Free FrGeCl3 perovskite solar cell using DFT and SCAPS-1D," *Inorganic Chemistry Communications*, vol. 171, p. 113578, Jan. 2025, doi: 10.1016/j.inoche.2024.113578.

[20] M. Al Atem and Y. Makableh, "Towards Sustainable Perovskite Solar Cells: Lead-Free High Efficiency Designs with Tin and Germanium," *Eng*, vol. 6, no. 2, p. 38, Feb. 2025, doi: 10.3390/eng6020038.

[21] F.-T.- Zahra, M. M. Hasan, Md. B. Hossen, and Md. R. Islam, "Deep insights into the optoelectronic properties of AgCdF3-based perovskite solar cell using the combination of DFT and SCAPS-1D simulation," *Heliyon*, vol. 10, no. 13, p. e33096, Jul. 2024, doi: 10.1016/j.heliyon.2024.e33096.

[22] M. K. Hossain *et al.*, "Numerical modeling and performance evaluation of non-toxic Cs2TiF6 based perovskite solar cells: A SCAPS-1D simulation study," *Journal of Physics and Chemistry of Solids*, vol. 203, p. 112734, Aug. 2025, doi: 10.1016/j.jpcs.2025.112734.

[23] M. Baro and P. Borgohain, "Design and performance analysis of Cs 2 Ag (Sb y Bi 1 - y) Br 6 perovskite solar cells: Insights from SCAPS-1D device simulations," *Renewable Energy*, vol. 256, p. 124225, Jan. 2026, doi: 10.1016/j.renene.2025.124225.

[24] M. K. A. Mohammed *et al.*, "Coupled DFT and SCAPS-1D investigation of a novel small-molecule for organic solar cells," *RSC Adv.*, vol. 15, no. 37, pp. 30347–30359, 2025, doi: 10.1039/D5RA04889C.

[25] M. U. N. Tariq *et al.*, "Optimization of high-efficiency solid-state dye sensitized solar cells (ssDSSCs) based on N719 dye via electron transport layer engineering using SCAPS-1D," *Results in Engineering*, vol. 27, p. 106465, Sep. 2025, doi: 10.1016/j.rineng.2025.106465.

[26] S. M. G. Mostafa *et al.*, "Device engineering and performance analysis of Cs2AgSbBr6 perovskite solar cells using SCAPS-1D," *Inorganic Chemistry Communications*, vol. 178, p. 114636, Aug. 2025, doi: 10.1016/j.inoche.2025.114636.

[27] A. D. K. Kenfack and M. Msimanga, "Effect of low-cost hole transport layers (HTLs) on the performance parameters of lead-free homojunction CsGeI2Br-based perovskite solar cells," *Next Materials*, vol. 6, p. 100482, Jan. 2025, doi: 10.1016/j.nxmate.2024.100482.

[28] C.-H. Peng and Y.-C. Lin, "SCAPS-1D Simulation of Various Hole Transport Layers' Impact on CsPbI2Br Perovskite Solar Cells Under Indoor Low-Light Conditions," *Solids*, vol. 6, no. 3, p. 31, Jun. 2025, doi: 10.3390/solids6030031.

[29] E. A. Nyiekaa, T. A. Aika, E. Danladi, C. E. Akhabue, and P. E. Orukpe, "Simulation and optimization of 30.17% high performance N-type TCO-free inverted perovskite solar cell using inorganic transport materials," *Sci Rep*, vol. 14, no. 1, p. 12024, May 2024, doi: 10.1038/s41598-024-62882-7.

[30] M. T. Islam and M. Sk, "Exploring the photovoltaic potential of $CuSbS_2$ using SCAPS-1D and DFT simulations," *Phys. Scr.*, vol. 100, no. 2, p. 025911, Feb. 2025, doi: 10.1088/1402-4896/ada20e.

[31] K. Thomas, A. Rahman, A. Khandakar, P. Chelvanathan, B. Aissa, and M. I. Hossain, "Optimizing Light Management in Bifacial Perovskite

Solar Cells Using Silica-Based Anti-Dust and Anti-Reflection Coatings for Harsh Environments," *Processes*, vol. 13, no. 2, p. 578, Feb. 2025, doi: 10.3390/pr13020578.
[32] S. Abdo *et al.*, "Unveiling the Potential of Novel Ternary Chalcogenide SrHfSe3 for Eco-Friendly, Self-Powered, Near-Infrared Photodetectors: A SCAPS-1D Simulation Study," *Sci*, vol. 7, no. 3, p. 113, Aug. 2025, doi: 10.3390/sci7030113.
[33] A. Ghosh *et al.*, "Enhancement of sulfide-based absorber and charge transport layer solar cell performance using machine learning and the SCAPS-1D simulator," *Phys. Chem. Chem. Phys.*, vol. 27, no. 29, pp. 15645–15668, 2025, doi: 10.1039/D5CP01664A.
[34] V. Leela Devi, P. Kuchhal, D. De, A. Sharma, N. Kumar Shukla, and M. Aggarwal, "Machine Learning-Driven Optimization of Transport Layers in $MAPbI_3$ Perovskite Solar Cells for Enhanced Performance," *IEEE Access*, vol. 12, pp. 179546–179565, 2024, doi: 10.1109/ACCESS.2024.3492378.
[35] L. Mdleleni, S. Mlala, T. Naki, E. L. Meyer, M. A. Agoro, and N. Rono, "Simulation of Perovskite Solar Cell with BaZr(S0.6Se0.4)3–Based Absorber Using SCAPS–1D," *Processes*, vol. 14, no. 1, p. 87, Dec. 2025, doi: 10.3390/pr14010087.
[36] F. Hao, C. C. Stoumpos, D. H. Cao, R. P. H. Chang, and M. G. Kanatzidis, "Lead-free solid-state organic–inorganic halide perovskite solar cells," *Nature Photon*, vol. 8, no. 6, pp. 489–494, Jun. 2014, doi: 10.1038/nphoton.2014.82.
[37] J. Hakami, "A comprehensive study to optimize organic/inorganic ETL and HTL materials on double perovskite layer Cs2AgBiBr6 solar cells with SCAPS 1D simulator," *Results in Engineering*, vol. 25, p. 104044, Mar. 2025, doi: 10.1016/j.rineng.2025.104044.
[38] X. Li, D. Jin, Q. Yu, and J. Zhao, "Simulated annealing algorithm-assisted SCAPS-1D design enables 27.04 % efficiency in dual-absorber perovskite solar cells," *Journal of Physics and Chemistry of Solids*, vol. 207, p. 112953, Dec. 2025, doi: 10.1016/j.jpcs.2025.112953.
[39] A. N. Khan, M. Kaleem, N. U. Khan, A. Nasir, A. Khan, and M. Z. Abbasi, "Multi-functional DFT and SCAPS-1D analysis of lead-free Z2MgGeI6 (Z = Na, K) double perovskites for optoelectronic, photo-catalytic, and photovoltaic applications," *Solar Energy Materials and Solar Cells*, vol. 294, p. 113922, Jan. 2026, doi: 10.1016/j.solmat.2025.113922.
[40] K. Gamal, M. Gamal, A. Okaz, N. Shehata, and I. Kandas, "Comprehensive performance analysis of perovskite solar cells based on different crystalline structures of MAPbI3," *Opt Quant Electron*, vol. 56, no. 5, p. 827, Mar. 2024, doi: 10.1007/s11082-024-06655-6.
[41] N. W. Hoy, L. L. Noto, and P. S. Mbule, "SCAPS-1D simulation of perovskite solar cells with hydroxyapatite scaffold for lead encapsulation and performance optimization," *Next Materials*, vol. 9, p. 101260, Oct. 2025, doi: 10.1016/j.nxmate.2025.101260.
[42] P. Bhuvaneswari and P. Sriramalakshmi, "A numerical approach of HTL-free FA0.75Cs0·25SnI3/KSnI3 based heterojunction perovskite solar cell with various ETLs and HTLs using SCAPS-1D," *Journal of Physics and Chemistry of Solids*, vol. 209, p. 113245, Feb. 2026, doi: 10.1016/j.jpcs.2025.113245.
[43] V. S and S. G, "Simulation strategy to amplify the opto-electrical output of MASnI3 perovskite solar cells by optimizing the charge extraction layers via SCAPS-1D," *Surfaces and Interfaces*, vol. 73, p. 107458, Sep. 2025, doi: 10.1016/j.surfin.2025.107458.
[44] D. B. C and P. Sriramalakshmi, "Simulation of lead free heterojunction n-FASnI3/p-FrGeCl3 based Perovskite solar cell with ZnMgO as Electron transport layer and GO as Hole transport layer using SCAPS-1D," *Results in Engineering*, vol. 27, p. 106180, Sep. 2025, doi: 10.1016/j.rineng.2025.106180.
[45] E. L. Meyer, S. Jakalase, A. Nqombolo, N. Rono, and M. A. Agoro, "The Numerical Simulation of a Non-Fullerene Thin-Film Organic Solar Cell with Cu2FeSnS4 (CFTS) Kesterite as a Hole Transport Layer Using SCAPS-1D," *Coatings*, vol. 15, no. 3, p. 266, Feb. 2025, doi: 10.3390/coatings15030266.
[46] R. R. Lekshmy, E. Raza, Z. Ahmad, and J. Bhadra, "Simulation and optimization of lead-free CH3NH3SnI3 perovskite solar cells using SCAPS-1D," *Results in Optics*, vol. 21, p. 100823, Dec. 2025, doi: 10.1016/j.rio.2025.100823.
[47] G. K. Kulkarni, S. S. Mali, J. V. Patil, A. S. Mali, P. M. Kodam, and C. K. Hong, "Unveiling the impact of cesium doping and functionalized carbon nanotubes on CsxFA1-xPbI3 performance: Insights from SCAPS-1D simulations," *Solar Energy*, vol. 299, p. 113698, Oct. 2025, doi: 10.1016/j.solener.2025.113698.
[48] S. A. Dar and B. S. Sengar, "Analysis of lead free $CsSnBr_3$ based perovskite solar cells utilizing numerical modeling," *Phys. Scr.*, vol. 99, no. 6, p. 065013, Jun. 2024, doi: 10.1088/1402-4896/ad43c7.
[49] S. Ullah *et al.*, "Optimization of mixed valence Cs2Au2I6-based double perovskite solar cells by SCAPS-1D simulation," *Journal of Physics and Chemistry of Solids*, vol. 208, p. 113192, Jan. 2026, doi: 10.1016/j.jpcs.2025.113192.
[50] B. V. Kheswa, S. N. T. Majola, H. Al-Dmour, N. M. Ndzane, and L. Makhathini, "Modeling and Analysis of KSnI3 Perovskite Solar Cells Yielding Power Conversion Efficiency of 30.21%," *Nanomaterials*, vol. 15, no. 8, p. 580, Apr. 2025, doi: 10.3390/nano15080580.
[51] X. Li and J. Zhao, "Towards 30.78 % efficiency: SCAPS-1D and genetic algorithm-assisted design of dual-absorber perovskite solar cells," *Materials Today Communications*, vol. 45, p. 112406, Apr. 2025, doi: 10.1016/j.mtcomm.2025.112406.
[52] E. Paz Totolhua *et al.*, "Enhanced Efficiency of Mixed-Halide Perovskite Solar Cells Through Optimization of the Layer Thicknesses, Defect Density, and Metal Contact Work Function," *Materials*, vol. 18, no. 7, p. 1601, Apr. 2025, doi: 10.3390/ma18071601.
[53] L. Xu *et al.*, "Vapor incubation of $FASnI_3$ films for efficient and stable lead-free inverted perovskite solar cells," *J. Mater. Chem. A*, vol. 9, no. 31, pp. 16943–16951, 2021, doi: 10.1039/D1TA04722A.
[54] P. Cui *et al.*, "Planar p–n homojunction perovskite solar cells with efficiency exceeding 21.3%," *Nat Energy*, vol. 4, no. 2, pp. 150–159, Feb. 2019, doi: 10.1038/s41560-018-0324-8.
[55] W. Zhao *et al.*, "TiO2 Electron Transport Layer with p–n Homojunctions for Efficient and Stable Perovskite Solar Cells," *Nano-Micro Lett.*, vol. 16, no. 1, p. 191, Dec. 2024, doi: 10.1007/s40820-024-01407-3.
[56] A. D. K. Kenfack, N. M. Thantsha, and M. Msimanga, "Simulation of Lead-Free Heterojunction CsGeI2Br/CsGeI3-Based Perovskite Solar Cell Using SCAPS-1D," *Solar*, vol. 3, no. 3, pp. 458–472, Aug. 2023, doi: 10.3390/solar3030025.
[57] K. P. Mishra, B. K. Pandey, and S. Pandey, "Unveiling the potential of FASnI3 solar cells through advanced charge transport materials: A SCAPS-1D perspective," *Journal of Alloys and Compounds*, vol. 1006, p. 176283, Nov. 2024, doi: 10.1016/j.jallcom.2024.176283.
[58] P. Bhuvaneswari and P. Sriramalakshmi, "Lead-Free p-n Homojunction Cs-Doped and Pure $FASnI_3$-based perovskite solar cells–a performance analysis using SCAPS 1D simulator," *Results in Engineering*, vol. 26, p. 104779, Jun. 2025, doi: 10.1016/j.rineng.2025.104779.
[59] M. K. Hasan, M. S. I. Sagor, J. A. Bhuiyan, H. Korucu, H. Mamur, and M. R. A. Bhuiyan, "Performance evaluation of al/ETLs/FASnI3/GO/Au PSCs using numerical and machine learning approaches," *Next Chemical Engineering*, vol. 2, p. 100016, Jun. 2026, doi: 10.1016/j.nxcen.2025.100016.

Md. Abid Morshed was born in Bogura, Bangladesh. He earned his bachelor's (B.Sc.) degree in Electrical and Electronic Engineering from American International University-Bangladesh (AIUB). In addition, he is now attending AIUB to pursue a master's degree (M.Sc.) in Electrical and Electronic Engineering. He is now working as a Teaching Assistant (TA) in the Faculty of Engineering (FE) at American International University-Bangladesh (AIUB), beginning in November 2024.

Mohammad Abdul Mannan was born in Laxmipur, Bangladesh on January 01, 1975. He received his B.Sc. Eng. Degree from Rajshahi University of Engineering and Technology (RUET former BITR), Bangladesh, in 1998, and Masters of Eng. and Dr. of Eng. degrees from Kitami Institute of Technology, Japan, in 2003 and 2006, respectively,

all in electrical engineering. He then joined in the American International University Bangladesh (AIUB) as an Assistant professor in May 2006. He served in AIUB as an Associate Professor from December 2013 to November 2016. Now he is working as a Professor and Associate Dean of the Faculty of Engineering in AIUB. His research interests include electric motor drive, power electronics, power system, wind generation system and control of electric motor, power electronic converters, power system, and wind generation system. Prof. Dr. Mannan is a senior member of the IEEE and fellow of IEB.

Dr. Md. Rifat Hazari received his B.Sc. and M.Sc. degrees in Electrical and Electronic Engineering from the American International University-Bangladesh (AIUB) in August 2013 and December 2014, respectively and Ph.D. degree in Energy Engineering from the Kitami Institute of Technology (KIT), Japan, in March 2019. He has held various academic and administrative positions at AIUB, including Senior Assistant Professor, Assistant Professor and Lecturer in the Department of Electrical and Electronic Engineering (EEE), and Deputy Director of the Dr. Anwarul Abedin Institute of Innovation, AIUB. He is currently serving as an Associate Professor and Special Assistant in the EEE Department at AIUB. Throughout his career, Dr. Hazari has received several prestigious recognitions, including the MINT (Academic Excellence) Award from KIT, Japan in 2017 for outstanding research performance, the Best Paper Award at the Australasian Universities Power Engineering Conference 2017 in Melbourne, Australia, the Best Presentation Award at the IEEJ Branch Convention 2017 in Hakodate, Japan, and the Best Sustainable Development Goal (SDG) Posterity Award at the 3rd International Conference on Robotics, Electrical and Signal Processing Techniques 2023 in Dhaka, Bangladesh. He has served as a Co-Principal Investigator (Co-PI) on multiple internationally funded research projects and has authored over 75 publications in peer-reviewed journals and national and international conferences. He has also been invited as a speaker at various universities and workshops. His research interests include renewable energy systems (particularly wind and photovoltaic power systems), power system stability and control, microgrid and hybrid power systems, HVDC system, analysis and control of rotating electrical machines. He is a member of both the Institute of Electrical and Electronics Engineers (IEEE) and the Institution of Engineers, Bangladesh (IEB).